HEALTH AND MEDICINE

Antibacterial infection and immune-evasive coating for orthopedic implants

Kyomin Chae[1]*, Woo Young Jang[2]*, Kijun Park[1]*, Jinhyeok Lee[2], Hyunchul Kim[1], Kyoungbun Lee[3], Chang Kyu Lee[4], Yeontaek Lee[1], Soon Hyuck Lee[2†], Jungmok Seo[1†]

Bacterial infection and infection-induced immune response have been a life-threatening risk for patients having orthopedic implant surgeries. Conventional biomaterials are vulnerable to biocontamination, which causes bacterial invasion in wounded areas, leading to postoperative infection. Therefore, development of anti-infection and immune-evasive coating for orthopedic implants is urgently needed. Here, we developed an advanced surface modification technique for orthopedic implants termed lubricated orthopedic implant surface (LOIS), which was inspired by slippery surface of *Nepenthes* pitcher plant. LOIS presents a long-lasting, extreme liquid repellency against diverse liquids and biosubstances including cells, proteins, calcium, and bacteria. In addition, we confirmed mechanical durability against scratches and fixation force by simulating inevitable damages during surgical procedure ex vivo. The antibiofouling and anti-infection capability of LOIS were thoroughly investigated using an osteomyelitis femoral fracture model of rabbits. We envision that the LOIS with antibiofouling properties and mechanical durability is a step forward in infection-free orthopedic surgeries.

INTRODUCTION

Nowadays, the number of patients who suffer from orthopedic diseases such as elderly bone fracture, degenerative joint disease, and osteoporosis has substantially increased because of global aging (*1*, *2*). Consequently, orthopedic implants including screws, plates, nails, and artificial joints have become highly sought after by health care institutions for orthopedic surgeries (*3*, *4*). However, the conventional orthopedic implants have been reported to be vulnerable to bacterial adhesion and biofilm formation, which can cause surgical site infection (SSI) after surgery (*5*, *6*). Once the biofilm has formed on the surface of the orthopedic implant, its removal becomes extremely difficult even with large doses of antibiotics. Thus, it usually results in severe postoperative infection (*7*, *8*). Because of the issues described above, the treatment of infected implants should involve reoperation, which includes removing all of the implants and the surrounding tissues; thus, the patients suffer from severe pain and several risks (*9*, *10*).

To address some of these problems, drug-eluting orthopedic implants have been developed to prevent infection by eradicating bacteria attached to the surface (*11*, *12*). However, the strategy still displays multiple limitations. Long-term implantation of drug-eluting implants was reported to have caused damage to the surrounding tissues and cause inflammation, which could possibly lead to necrosis (*13*, *14*). In addition, organic solvents that may be present after the manufacturing process of the drug-eluting orthopedic implant that are strictly prohibited by the U.S. Food and Drug Administration require additional purification steps to comply with its standards (*15*). The controlled release of drugs by drug-eluting implants

has been challenging, and its application for long-term usage is not feasible due to its limited drug-loading capacity (*16*).

Another common strategy involves coating the implants with an antibiofouling polymer, which prevents biosubstances and bacteria from adhering onto the surface (*17*). For example, zwitterionic polymers have received attention because of their nonadhesive properties when in contact with plasma proteins, cells, and bacteria. However, it has several limitations relating to long-term stability and mechanical durability, which hinder practical applications in orthopedic implants, especially since mechanical scratching occurs during surgical operations (*18*, *19*). In addition, orthopedic implants made of biodegradable materials have been adopted because of its high biocompatibility, lack of necessity for removal surgery, and surface-cleaning property via erosion (*20*, *21*). While in erosion, the chemical bond between the polymeric matrix gets broken down and detached from the surface with its adherent cleaning its surface. However, the antibiofouling via surface cleaning is effective in the short term. Moreover, most of the resorbable materials including poly(lactic-co-glycolic acid) (PLGA), polylactic acid (PLA), and magnesium-based alloy undergo nonuniform biodegradation and erosion in the body, negatively affecting the mechanical stability (*22*). In addition, the biodegraded plate debris provide site for bacterial adhesion, increasing a chance of infection in the long term. Such mechanical degradation and infection risk limit the practical applications in orthopedic surgery (*23*).

Superhydrophobic (SHP) surfaces, which mimic the hierarchical structure of a lotus leaf, have emerged as a potential solution for antibiofouling surfaces (*24*, *25*). When SHP surfaces are submerged in liquid, air bubbles become trapped, therefore forming air pockets and preventing bacterial adhesion (*26*). However, recent studies suggest that SHP surfaces have shortcomings relating to mechanical durability and long-term stability, which hinder its application to medical implants. Moreover, the air pockets get dissolved, losing the antibiofouling property and, consequently, leading to more extensive bacterial adhesion due to the large surface area of the SHP surfaces (*27*, *28*). Recently, Aizenberg and colleagues introduced an innovative approach to antibiofouling surface coating by developing

[1]School of Electrical and Electronic Engineering, Yonsei University, Seoul 03722, Republic of Korea. [2]Department of Orthopedic Surgery, Korea University Anam Hospital, Seoul 02841, Republic of Korea. [3]Department of Pathology, Seoul National University College of Medicine, Seoul 03080, Republic of Korea. [4]Department of Laboratory Medicine, Korea University Anam Hospital, Seoul 02841, Republic of Korea.
*These authors contributed equally to this work.
†Corresponding author. Email: jungmok.seo@yonsei.ac.kr (J.S.); soonlee@korea.ac.kr (S.H.L.)

a slippery surface inspired by the *Nepenthes* pitcher plant (*29*, *30*). The slippery surface shows long-term stability under liquid pressure conditions, extreme liquid repellent for biological liquids, and a self-healing property. However, there has neither been any approach, which applies the coating on complex-shaped medical implants nor demonstrates a healing process of supporting damaged tissues after its implantation.

Here, we introduce a lubricated orthopedic implant surface (LOIS), a micro/nanostructured orthopedic implant surface tightly combined with a thin lubricant layer, to prevent bacterial infections associated with orthopedic surgery such as fracture fixation. Because of fluorine-functionalized micro/nano-hierarchical structures that firmly hold lubricants on the structure, the developed LOIS can fully repel the adhesion of various liquids and maintain the antibiofouling properties for a long period of time. The LOIS coating can be applied to various materials of different shapes that are intended for osteosynthesis. LOIS' exceptional antibiofouling property against biofilm bacteria [*Pseudomonas aeruginosa* and methicillin-resistant *Staphylococcus aureus* (MRSA)] and biosubstances (cells, proteins, and calcium) was confirmed in vitro, resulting in less than 1% attachment where extensive adhesion occurred in bare substrate. In addition, self-healing due to the infiltrated lubricant helped in maintaining its antibiofouling property even after mechanical stress such as scratching on the surface occurred. The mechanical durability test results showed the insignificant degradation in the overall strength even after structural and chemical modification. In addition, ex vivo experiment simulating mechanical stresses present in surgical environment was conducted to demonstrate that LOIS can endure various mechanical stresses that occur during orthopedic surgery. Last, we demonstrated the superior antibacterial property and biocompatibility of LOIS using an in vivo femoral fracture model based on rabbits. Stable lubricant behavior and antibiofouling properties over 4 weeks of implantation allowed effective anti-infection and immune-evasive performance without a delay in the bone healing process, which were confirmed by radiographic and histology results.

RESULTS

Figure 1A shows the schematic of a developed LOIS with micro/nano-hierarchical structures implanted in the rabbit femoral fracture model to confirm its excellent antibiofouling and anti-infection property. Biomimetic approach was conducted to mimic the surface of the pitcher plant and to prevent biofouling by combining a lubricant layer within the micro/nanostructure of the surface. The lubricant-infused surface minimizes the contact between the biosubstances and the surface, therefore allowing exceptional antibiofouling property and demonstrating long-term stability because of stable chemical bonding being formed on the surface. As a result, the antibiofouling property of the lubricated surface allows various practical applications in biomedical research. However, extensive studies on how this exceptional surface interacts in vivo still remain undone. The nonadhesive property of the LOIS was confirmed by comparing it to the bare substrate in vitro using albumin and biofilm bacteria (Fig. 1B). In addition, the biofouling performance was demonstrated by rolling off the blood droplets on the tilted bare substrates and LOIS substrates (fig. S1 and movie S1). As shown in the fluorescence microscopy images, the bare substrate incubated in protein and bacterial suspension demonstrated a large number of biosubstances adhering on the surface. However, LOIS hardly showed any fluorescence due to its excellent antibiofouling property. To confirm the antibiofouling property and anti-infection property, LOIS was applied on the surface of orthopedic implants for osteosynthesis (plate and screws) and was placed in the rabbit fracture model. Before implantation, both bare orthopedic implants, and LOIS was incubated in the bacterial suspension for 12 hours. The preincubation ensures that a biofilm is formed on the surface of the
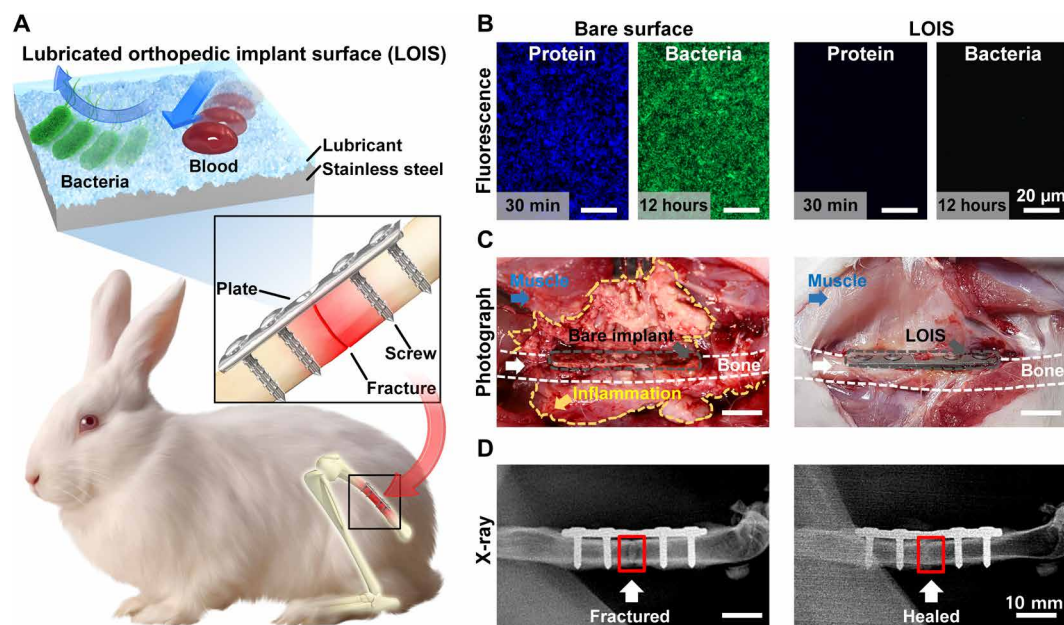

Fig. 1. LOIS for antibiofouling orthopedic implants. (**A**) Schematics of the LOIS and its implantation in rabbit femoral fracture model. (**B**) Fluorescence microscopy images of protein and bacterial biofilm on bare surface and LOIS substrate. (**C**) Photograph images and (**D**) x-ray images of the fracture site (highlighted with red rectangle) 4 weeks after implantation. Photo credit: Kyomin Chae, Yonsei University.

bare implant for comparison. Figure 1C shows the photograph of the fracture site after 4 weeks of implantation. On the left side, rabbits implanted with the bare orthopedic implants demonstrated serious levels of inflammation because of the biofilm formed on the implant surface. The opposite results were observed in the rabbits implanted with LOIS that the surrounding tissues of LOIS showed neither signs of infection nor inflammation. In addition, an optical image on the left, which indicates the surgical site of the rabbit with bare implants, demonstrated that a variety of adherents present on the surface of the bare implant were not found on the surface of LOIS. This indicates that LOIS has long-term stability and a capacity to maintain its antibiofouling and anti-adhesion properties.

Sterilized bare-negative implanted rabbits demonstrated a regular bone healing process without any signs of inflammation and infection. On the other hand, SHP implants that were preincubated in bacterial suspension demonstrated an infection-associated inflammation on the surrounding tissues. This can be attributed to its inability to inhibit bacterial adhesion for a long period of time (fig. S2). To demonstrate that the LOIS does not affect the healing process, but inhibits possible infection associated with implantation, x-ray images on the fracture site were compared between bare-positive substrate and LOIS (Fig. 1D). X-ray images with the bare-positive implant showed persistent osteolytic line, indicating that the bone was not fully healed. This suggests that the bone recovery process could have been significantly delayed due to the infection-associated inflammation. On the contrary, the rabbit implanted with LOIS was shown to have healed, not demonstrating any site of clear fracture.

Numerous efforts have been made to develop medical implants with long-term stability and functionality including antibiofouling. However, in dynamic circumstances where various biosubstances and tissue adhesion exist have limited their development of clinically reliable method. To overcome these shortcomings, we developed a micro/nano-hierarchical structure and a chemically modified surface, which was optimized to maximally hold the slippery lubricant, which is due to high capillary force and chemical affinity. Figure 2A demonstrates the overall fabrication process of LOIS. First, the medical-grade stainless steel (SS) 304 substrate was prepared. Second, the micro/nanostructure was formed on the SS substrate via chemical etching using hydrofluoric acid (HF) solution. To restore the corrosion resistance property of the SS, the etched substrates were treated using nitric acid (HNO_3) solution (31). The passivation enhances the corrosion-resistant properties of the SS substrate, markedly slowing down the corrosion processes that could degrade the overall performance of LOIS. Then, the surface was chemically modified by forming a self-assembled monolayer (SAM) with 1H,1H,2H,2H-perfluorooctyltriethoxysilane (POTS) to increase the chemical affinity between the surface and slippery lubricant. The surface modifications markedly lowered the surface energy of the fabricated micro/nano-hierarchical structured surface, matching that of slippery lubricant. This allows complete wetting by the lubricant, forming a stable lubricant layer on the surface. The modified surface exhibited enhanced hydrophobicity. Results show that because of the high chemical affinity and capillary force induced by the micro/nanostructure, the slippery lubricant demonstrated a stable behavior on LOIS (32, 33). Optical changes to the SS surface following surface modification and lubricant infusion were investigated. The micro/nano-hierarchical structures formed on the surface causes visual changes that the surface become darker. The phenomenon is due to the enhanced light scattering effects on the rough surface that increases diffuse reflection

resulting from the light trapping mechanism (34). Moreover, the LOIS became even darker after lubricant infusion. The lubricant layer caused less light to be reflected from the substrate, darkening the LOIS. To optimize the micro/nanostructure to exhibit lowest sliding angle (SA) for antibiofouling properties, the fabricated structures with different etching time in HF (0, 3, 15, and 60 min) were characterized using scanning electron microscopy (SEM) and an atomic force microscope (AFM) (Fig. 2B). The SEM and AFM images demonstrated that the bare substrate formed uneven nanoscale roughness after a short etching period (3 min of etching). The changes in surface roughness depending on different etching time were investigated (fig. S3). The time-dependent plot suggests that the surface roughness continued to increase and reach the peak at 15 min of etching, and then only a slight decrease in the roughness value was observed at 30 min of etching. At the point, the nanoscale roughness gets etched away, while microscale roughness robustly develops, evening out the roughness changes. After more than 30 min of etching, another increase in roughness was observed, and the detail explanation is as the following: SS consists of steel, alloyed with elements including iron, chromium, nickel, molybdenum, and many other elements. Among these elements, iron, chromium, and molybdenum play an important role in the formation of micro/nanoscale roughness on SS via HF etching. At the early stage of etching, iron and chromium mainly get etched, as molybdenum has a higher corrosion resistance compared to them. As the etching proceeds, the etching solution reaches local supersaturation, forming etching-induced fluoride and oxides. The fluoride and oxides get precipitated and eventually redeposited on the surface, forming micro/nanoscale surface roughness (31). This micro/nanoscale roughness plays an important role in the self-healing properties of the LOIS. The dual-scale surface produces a synergistic effect that greatly increases the capillary force. This phenomenon allows the lubricants to stably infiltrate the surface and contribute to self-healing properties (35). The roughness formation depends on the etching time. Under 10-min etching, the surface only consists of nanoscale roughness, which is not adequate to hold enough lubricants for antibiofouling property (36). On the other hand, if the etching time exceeds 30 min, then the nanoscale roughness formed by the redeposition of iron and chromium disappears, while only microscale roughness, due to molybdenum, remains. The over-etched surface lacks nanoscale roughness and the synergistic effect of dual-scale roughness is lost, negatively influencing the self-healing properties of the LOIS. The SA measurement was performed on the substrate with different etching time to demonstrate the antibiofouling performance. The various types of liquids including deionized (DI) water, blood, ethylene glycol (EG), ethanol (EtOH), and hexadecane (HD) were selected on the basis of viscosity and surface energy (fig. S4). The etching time–dependent plot suggests that the LOIS etched for 15 min exhibited the lowest SA against various liquids with different surface energy and viscosity. Therefore, the LOIS was optimized to etch for 15 min to form both micro- and nanoscale roughness that is appropriate to hold the lubricants effectively for a durable and exceptional antibiofouling property.

Then, to confirm the changes in the chemical property of the surface, changes in the chemical composition of the substrate surface after each surface coating were investigated using x-ray photoelectron spectroscopy (XPS). Figure 2C shows the XPS measurement results of the HF-etched surface and HNO_3-treated surface. The two main peaks at 587.3 and 577.7 eV can be attributed to the
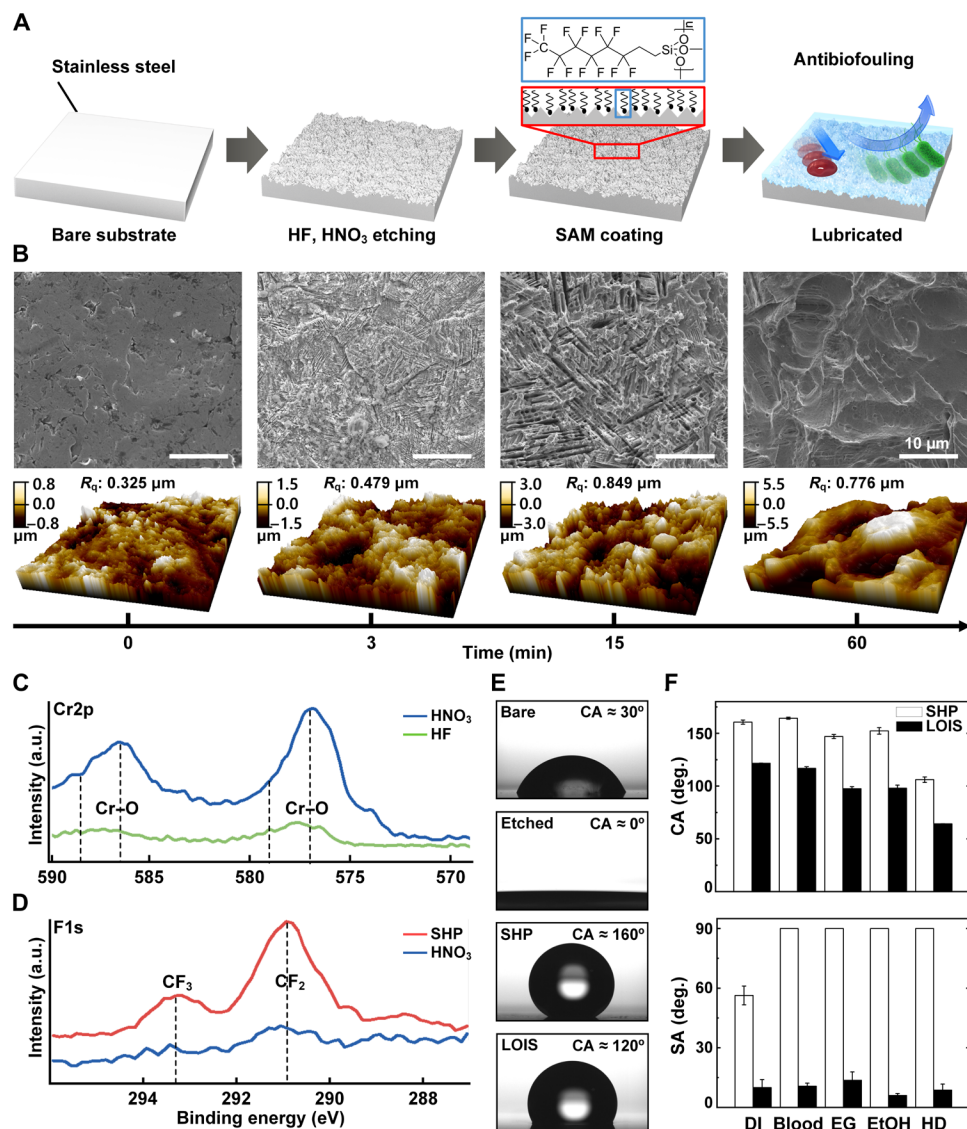
Fig. 2. Fabrication process of LOIS and its characterization. (**A**) Schematics of the four-step fabrication process of LOIS. The inset shows the SAM formed on the substrate. (**B**) SEM and AFM images for optimization of the micro/nanostructure of the substrate in different etching time. X-ray photoelectron spectroscopy (XPS) spectra of the (**C**) Cr2p and (**D**) F1s after surface passivation and SAM coating. a.u., arbitrary units. (**E**) Representative images of water droplet on bare, etched, SHP, and LOIS substrates. (**F**) Contact angle (CA) and SA measurement of liquids with different surface tension on SHP and LOIS. Data are presented as means ± SD.

Cr—O bonding present in the chromium oxide layer, which is the primary difference with the HF-etched surface. This is mainly due to HNO$_3$ consuming iron and chromium fluorides on the surface. The HNO$_3$–based etching allows chromium to form a passive oxide layer on the surface, which makes the etched SS resistant to corrosion once again. In Fig. 2D, XPS spectra was obtained to confirm the formation of fluorocarbon-based silane on the surface after the SAM coating, which exhibits extremely high liquid repellency even for EG, blood, and EtOH. The SAM coating was done by reacting the silane functional group with the hydroxyl group formed by plasma treatment. As a result, there was an observed notable increase in the CF$_2$ and CF$_3$ peaks. The binding energies between 286 and 296 eV suggest that the chemical modification was successfully done by the SAM coating. The SHP shows a relatively large CF$_2$ (290.1 eV) and CF$_3$ (293.3 eV) peaks, arising from the fluorocarbon-based silane formed on the surface. Figure 2E shows the representative optical images of the contact angle (CA) measurements of the different groups of DI water in contact with bare, etched, SHP, and LOIS. These images indicate that the etched surface became hydrophilic because the micro/nanostructure formed by chemical etching allowed DI water to be absorbed into the structure. However, when the substrate was coated with SAM, the substrate exhibited strong water repellency, therefore making the surface SHP and showing a smaller area of contact between the water and the surface. Last, the decrease of CA was observed in LOIS, which can be attributed to the infiltration of the lubricant into the microstructure, therefore increasing the area of contact. To demonstrate superior liquid repellency and nonadhesive property of the surface, LOIS was compared to the SHP substrate by measuring CA and SA using various liquids (Fig. 2F). The various types of liquids including DI water,

blood, EG, EtOH, and HD were selected on the basis of viscosity and surface energy (fig. S4). The CA measurement shows the decreasing value of CA as it gets toward HD, which has the lowest surface energy among them. In addition, the overall CA is comparably lower in LOIS. However, the SA measurement demonstrated completely different phenomenon. All the liquids except for DI water adhered to the SHP substrate without sliding off. On the other hand, LOIS demonstrated remarkably low SA, wherein all liquids rolled off when it was tilted at an angle below 10° to 15°. This strongly suggests that the nonadhesive property of LOIS is superior to that of the SHP surface. In addition, LOIS coating was applied to various types of materials including titanium (Ti), polyphenylsulfone (PPSU), polyoxymethylene (POM), polyetheretherketone (PEEK), and bioresorbable polymer (PLGA), which are alternative implantable orthopedic materials (fig. S5). Sequential images of blood droplet rolling off on the LOIS-treated materials suggest that the antibiofouling properties of the LOIS were consistent on all substrates. In addition, the CA and SA measurements demonstrate that the nonadhesive properties of LOIS can be applied to other materials.

To confirm the antibiofouling property of LOIS, various types of substrates including bare, etched, SHP, and LOIS were incubated with *P. aeruginosa* and MRSA. These two bacteria were selected as representative hospital bacteria, which cause biofilm formation, leading to SSI (*37*). Figure 3 (A and B) demonstrate the fluorescence microscopy images and colony-forming unit (CFU) measurements for the substrates incubated in bacterial suspension for a short (12 hours) and long (72 hours) term, respectively. In the short term, the bacteria form clusters and grow in size, encapsulating themselves with mucoid material and hindering its removal. However, in the 72-hour incubation, the bacteria mature and become ready to disperse to form additional colonies or clusters. Thus, the 72-hour incubation can be considered long term and is an appropriate incubation time to form vigorous biofilm on the surface (*38*). The etched and SHP surfaces demonstrated bacterial adhesion with approximately 25 to 50% less adherence compared to the bare substrate in the short term. However, LOIS showed no bacterial biofilm adherence in both the short and long term due to its excellent antibiofouling property and stability. The explanation of the antibiofouling mechanism for etched, SHP, and LOIS was described in the schematic (Fig. 3C). The hypothesis was that the etched substrate that exhibits hydrophilic property will have a larger surface area compared to that of the bare substrate; thus, more bacterial adhesion will occur on the etched substrate. However, the etched substrate had visibly less biofilm formed on the surface compared to that of the bare substrate. This is because the water molecule strongly binds to the hydrophilic surface and works as a water lubricant, therefore disturbing the bacterial attachment in the short term (*39*). However, the water molecular layer is very thin and soluble in bacterial suspension. Thus, the water molecular layer disappears in the long term, leading to extensive bacterial adhesion and proliferation. For SHP, the bacterial adhesion was inhibited because of its nonwetting property in the short term. The lowered bacterial adhesion can be attributed to the air pockets trapped in the hierarchical structure with low surface energy, which minimizes the contact between the bacterial suspension and the surface. However, extensive bacterial adhesion was observed in SHP, as it lost its antibiofouling property in the long term. This is mainly due to the air pockets disappearing because of hydrostatic pressure and the dissolution of air gas in water, which is mainly due to the air pockets disappearing by dissolution

and the hierarchical structure providing larger surface area for adhesion (*27*, *40*). Unlike these two substrates in which long-term stability matters, LOIS contains slippery lubricants infused in the micro/nanostructures, which do not disappear even in the long term. The lubricant filling the micro/nanostructure is very stable and is strongly attracted to the surface because of its high chemical affinity, which prevents bacterial adhesion for the long term. Figure S6 demonstrates the reflection confocal microscopy images of the lubricant-infused substrate submerged in phosphate-buffered saline (PBS). The sequential images suggest that the lubricant layer on the LOIS was maintained even after 120 hours of mild shaking (120 rpm), demonstrating long-term stability under flow. This is due to the high chemical affinity between the fluorine-based SAM coating and perfluorocarbon-based lubricant enabling the formation of a stable lubricant layer. Therefore, the antibiofouling performance was maintained. In addition, the substrates were tested against representative proteins (albumin and fibrinogen), which are found to be in high concentration in blood plasma, cells (macrophage and fibroblast) that are closely related to immune function, and calcium that is involved in bone formation (Fig. 3D, 1 and 2, and fig. S7) (*41*, *42*). In addition, fluorescence microscopy images for fibrinogen, albumin, and calcium adhesion tests demonstrated different adhesive properties of each substrate group (fig. S8). In the bone generation process, the newly formed bone and calcium layer might surround the orthopedic implants, which not only makes the removal difficult but may also potentially inflict unintended harm to the patients during removal. Thus, low level of calcium deposition on bone plates and screws is beneficial for orthopedic surgeries, which require removal of the implants. On the basis of the fluorescence intensity–based quantification of adhered area and cell counting, we confirmed that LOIS exhibits superior antibiofouling property against all the biosubstances compared to the other substrates. On the basis of the in vitro experiment results, the antibiofouling LOIS could be applied to orthopedic implants for osteosynthesis that do not only inhibit infection induced by the biofilm bacteria but also reduce inflammation caused by the active immune system of the body.

Mechanical durability has been a major challenge to the application of antibiofouling coating where inevitable and concentrated stresses are applied. Traditional antibiofouling hydrogel approaches are based on polymers with low water solubility and high fragility. Thus, they are often vulnerable to mechanical stresses in biomedical applications. Therefore, mechanically durable antibiofouling coating still remains as a challenge for applications such as orthopedic implants (*43*, *44*). Figure 4A (1) demonstrates the two major types of stresses applied to the orthopedic implants, which include scratch (shear stress) and compression induced by forceps with optical images of the damaged implant. For example, orthopedic plates get damaged and scratched in both the macro- and micro/nanoscale when the screws are fastened with a driver or when a surgeon tightly holds the plate with forceps and, thus, applying compressive force (Fig. 4A, 2). To test whether the fabricated LOIS could endure these damages during the orthopedic surgery, nanoindentation was performed to compare the hardness of bare substrate and LOIS in micro/nanoscale to investigate the influence of micro/nanostructures to its mechanical property (Fig. 4B). The schematics demonstrate different deformation behaviors of LOIS due to the micro/nanostructure present. The force-displacement curve was drawn on the basis of the nanoindentation results (Fig. 4C). The blue plot, which represents the bare substrate, shows only a slight deformation,
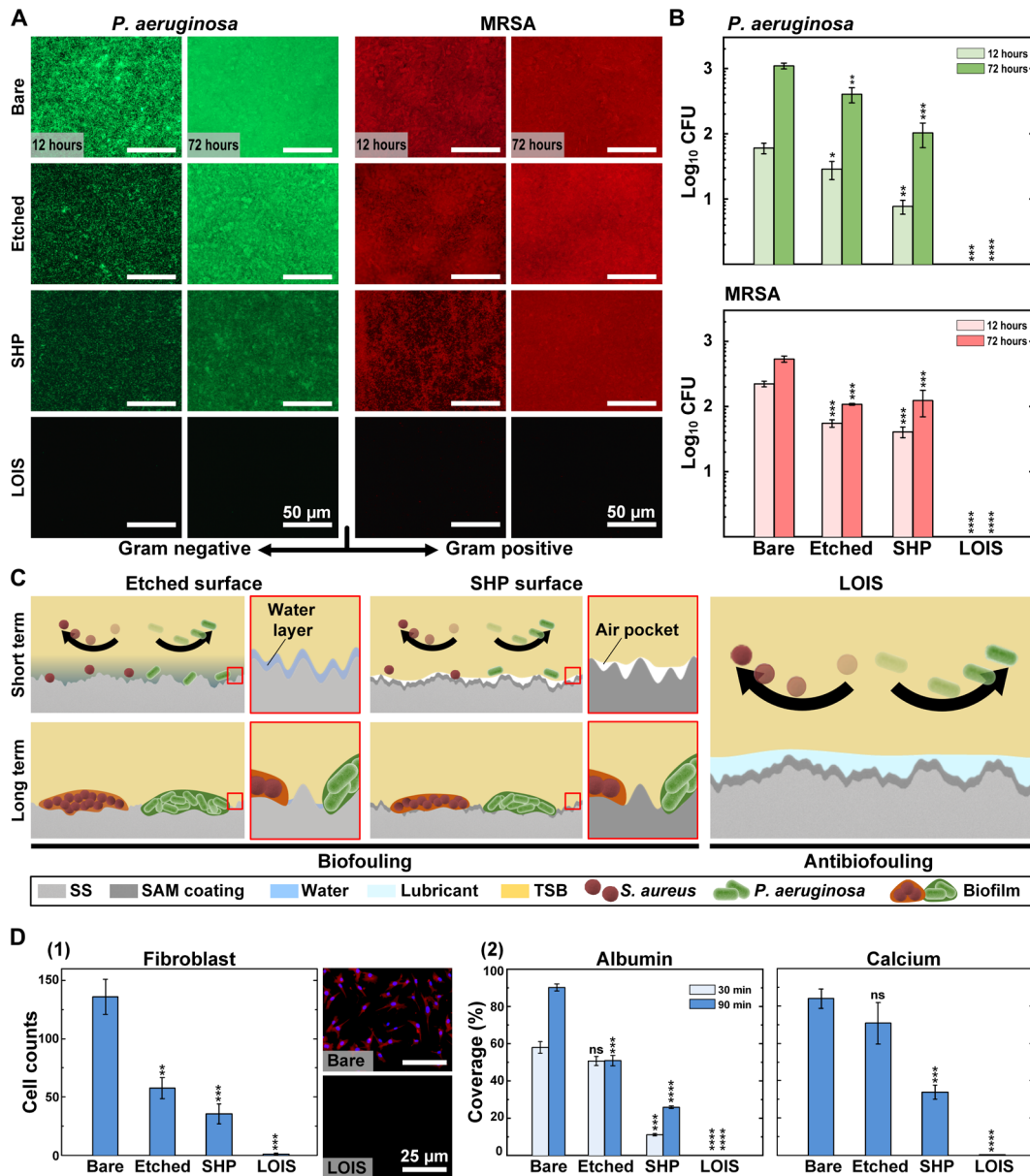
Fig. 3. Antibiofouling property of LOIS against bacteria, cell, protein, and calcium. (**A**) Fluorescence microscopy images of each group (bare, etched, SHP, and LOIS) incubated in *P. aeruginosa* and MRSA suspension for 12 and 72 hours. (**B**) The number of adherent CFUs of *P. aeruginosa* and MRSA on each group of surfaces. (**C**) Schematics for antibiofouling mechanism of etched, SHP, and LOIS in the short and long term. (**D**) (1) Number of fibroblasts adhered on each substrate and fluorescence microscopy images of the cells adhered on bare and LOIS. (2) Adhesion test for immune-related protein, albumin, and calcium involved in bone healing process (*$P < 0.05$, **$P < 0.01$, ***$P < 0.001$, and ****$P < 0.0001$). ns, not significant.

as seen with the 0.26-μm maximum indentation depth. On the other hand, the gradual increase in the nanoindentation force and displacement observed in LOIS (red plot) may show signs of degrading mechanical property, resulting in the nanoindentation depth of 1.61 μm. This is because the micro/nanostructure present in LOIS, which provides space for the nanoindenter tip to advance relatively deeper and, thus, causes greater deformation compared to that of the bare substrate. Konsta-Gdoutos *et al.* (*45*) suggested that nanoindentations and micro/nano-roughness result in an irregular nanoindentation curve because of the presence of a nanostructure. The shaded region corresponds to the irregular deformation curve attributed to the nanostructure, while the nonshaded region is due to the microstructure. This deformation may cause damages to the micro/nanostructures holding the lubricant and have negative effects to its antibiofouling property. To investigate the effects of the damages on LOIS, inevitable damages to micro/nanostructures during the orthopedic surgery was reproduced ex vivo. The stability of the antibiofouling property of the LOIS after ex vivo was confirmed by an adhesion test using blood and proteins (Fig. 4D). A series of optical images show the damages occurred near the holes in every substrate. Blood adhesion test was performed to demonstrate the effects of the mechanical damages to the antibiofouling
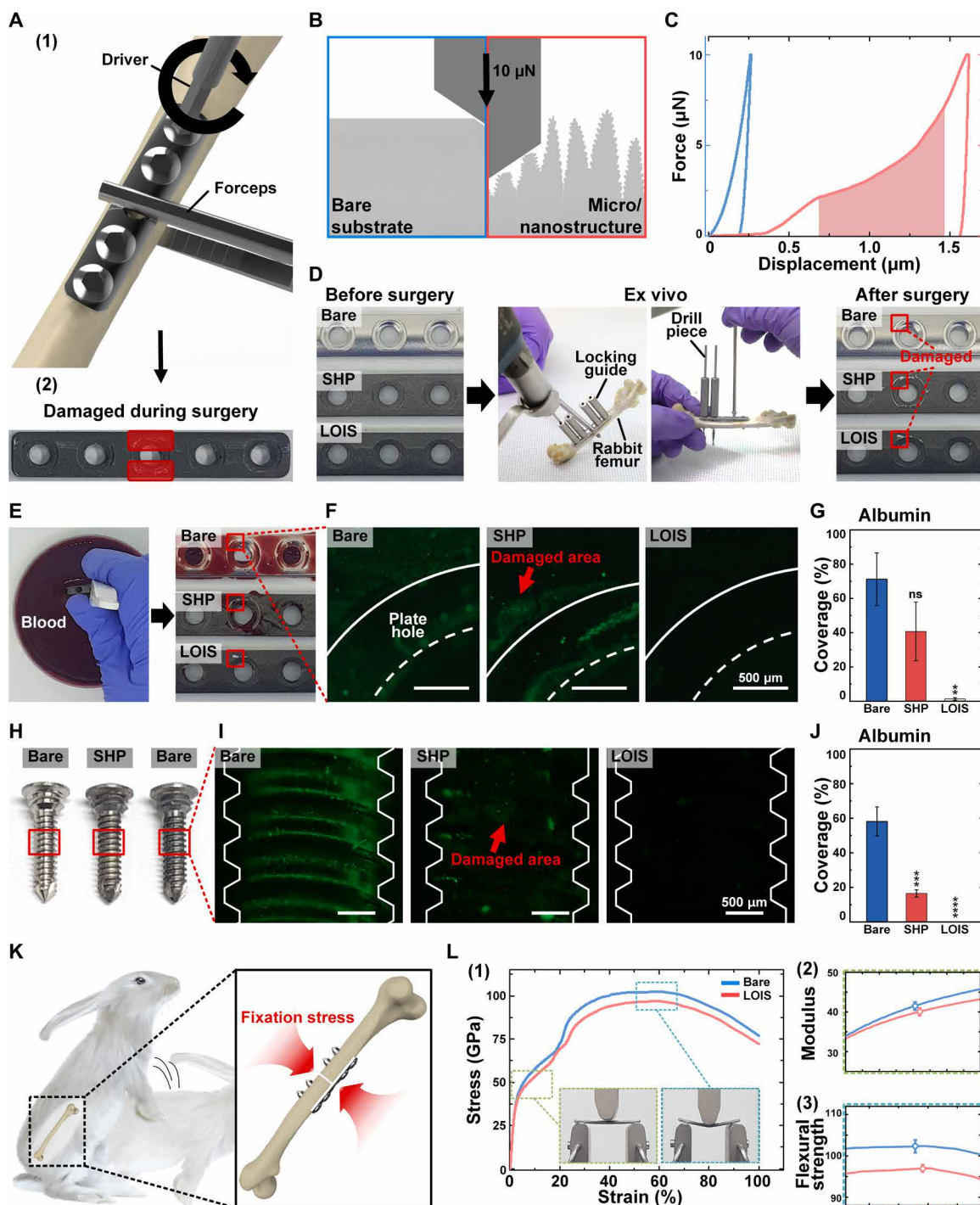
Fig. 4. Mechanical durability of LOIS. (**A**) Schematics of (1) mechanical stress applied on the orthopedic implants during surgery and (2) optical image of the damaged orthopedic implant. (**B**) Schematics of nanomechanical property measurement via nanoindentation on bare surface and LOIS. (**C**) Nanoindentation force-displacement curves of bare surface and LOIS. (**D**) Optical images (the damaged areas highlighted with red rectangle) of different types of the orthopedic plates after ex vivo experiment to simulate the mechanical stress–causing damages during surgery. (**E**) Blood adhesion test and (**F**) protein adhesion test for the damaged orthopedic plate groups. (**G**) Measurement of the area coverage of protein adhered on the plates. (**H**) Optical images of the different types of orthopedic screws after ex vivo experiment. (**I**) Protein adhesion test to investigate the intactness of the different coatings. (**J**) Measurement of the area coverage of protein adhered on the screws. (**K**) Schematics of the rabbit's movement, inducing fixation stress on fractured bone. (**L**) (1) Bending test results and optical images before and after bending. Difference of (2) Young's modulus and (3) flexural strength in bare implant and SHP. Data are presented as means ± SD (*$P < 0.05$, **$P < 0.01$, ***$P < 0.001$, and ****$P < 0.0001$). Photo credit: Kyomin Chae, Yonsei University.

coating (Fig. 4E). Unlike SHP, which lost its antibiofouling property due to the damage, LOIS exhibited superior antibiofouling property by repelling blood. This is because flow in the slippery lubricant infused with the microstructure due to the surface energy being driven by the capillary action that covers the damaged area recovering antibiofouling property (35). The same tendency was observed in the protein adhesion test using albumin. Adhesion of protein on the SHP surface was extensively observed in the damaged area, as half as bare substrate as the levels of adhesion were quantified by measuring its area coverage. On the other hand, LOIS maintained its antibiofouling property, which did not result in adhesion (Fig. 4, F and G). Furthermore, the surface of the screws is often subjected to intense mechanical stress, such as drilling, so we investigated the ability of the LOIS coating to remain intact on the screws ex vivo. Figure 4H shows the optical images of different screws including bare, SHP, and LOIS. The red rectangles indicate the areas of interest where intense mechanical stress occurs during implantation into the bone. Similar to the protein adhesion test for the plates, protein adhesion was imaged using a fluorescence microscope, and the area of coverage was measured to demonstrate the intactness of the LOIS coating even after intense mechanical stress (Fig. 4, I and J). LOIS-treated screws demonstrated excellent antibiofouling properties, resulting in few or no proteins adhering to the surface. On the other hand, protein adhesion was observed in bare and SHP screws, where the area coverage of SHP screws was one-third of the bare screw. Moreover, orthopedic implants for fixation must be mechanically robust to endure the stress applied onto the fracture site, as illustrated in Fig. 4K. Therefore, the bending test was conducted to determine the effects of the chemical modification on the mechanical property. In addition, this was done to sustain the fixation stress from the implant. The vertical mechanical force was applied until the implant was completely folded, and the stress-strain curve was obtained (Fig. 4L, 1). Two characteristics including Young's modulus and flexural strength were compared between the bare and LOIS substrate as an indicator of their mechanical strengths (Fig. 4L, 2 and 3). Young's modulus represents the ability of a material to withstand mechanical changes. The Young's modulus for each substrate was 41.48 ± 1.01 and 40.06 ± 0.96 GPa; the observed difference was approximately 3.4%. In addition, flexural strength, which determines the toughness of the material, was reported to be 102.34 ± 1.51 GPa for bare substrate and 96.99 ± 0.86 GPa for SHP; the bare substrate was approximately 5.3% higher. The subtle decrease of mechanical properties might be caused by notch effects in which the micro/nano-roughness might have worked as a population of notches, leading to the local concentration of stresses and affecting the implant's mechanical properties (46). However, based on the fact that the stiffness of human cortical bone is reported ranging from 7.4 to 31.6 GPa and the measured modulus of the LOIS exceeds that of human cortical bone (47), LOIS is strong enough to support bone fracture, and its overall mechanical properties were minimally affected by the surface modification.

In clinical cases, most of the bacterial contact with biomaterials and wound sites comes from well-established, mature biofilms (48). Consequently, the U.S. Centers for Disease Control and Prevention has estimated that 65% of all infections in humans are biofilm related (49). In this context, in vivo experimental design that provides consistency in biofilm formation on the implant surface was required. Therefore, we developed the rabbit femoral fracture model, in which orthopedic implants are preincubated in bacterial suspen-

sion and then implanted in a rabbit's femur to investigate the antibiofouling property of LOIS in vivo. The bacterial infection was induced by preincubation rather than direct injection of the bacterial suspension due to three important facts: (i) The immune system of rabbits are naturally more robust than those of humans; therefore, the injection of bacterial suspension and planktonic bacteria might be ineffective in forming biofilms; (ii) planktonic bacteria are more vulnerable to antibiotics, which are generally to be administered after surgery; last, (iii) planktonic bacterial suspension might be diluted by the bodily fluids of animals (50). By preincubating the implants in bacterial suspension before implantation, we were able to thoroughly investigate the harmful effects of bacterial infection and foreign body response (FBR) to the bone healing process. The rabbits were sacrificed 4 weeks after the implantation, as the bone union that is essential for the bone healing process finishes within 4 weeks. Then, the implants were removed from the rabbits for downstream investigation. Figure 5A demonstrates the proliferation mechanism of the bacteria; an infected orthopedic implant is introduced in the body. As a result of preincubation in the bacterial suspension, six of the six rabbits implanted with bare implants became infected, while none of the rabbits implanted with LOIS-treated implants were infected. The bacterial infection progresses in three steps including growth, maturation, and dispersion (51). First, the attached bacteria multiply and grow on the surface, and then the bacteria form the biofilm, as it excretes extracellular polymeric substances (EPS), amyloids, and extracellular DNAs. The biofilm not only interferes with the penetration of antibiotics but also facilitates the accumulation of antibiotic-degrading enzymes such as β-lactamases (52). Last, the biofilm disperses the matured bacteria to the surrounding tissues; consequently, infection occurs. In addition, infection that causes intense immune responses, which occur as foreign bodies get introduced into the body, can result in severe inflammation, pain, and degradation of immunity. Figure 5B provides an overview of the FBR due to insertion of orthopedic implants rather than the immune response caused by bacterial infection. The immune system recognizes the inserted implants as foreign bodies and then causes cellular and tissue response to encapsulate the foreign body (53). In the early step of FBR, the provision matrix was formed on the surface of orthopedic implants, leading to adsorption of fibrinogen. The adsorbed fibrinogen then forms a highly dense fibrin network that promotes the attachment of leukocytes (54). Once the fibrin network is formed, acute inflammation occurs due to the infiltration of neutrophils. In this step, various cytokines such as tumor necrosis factor–α (TNF-α), interleukin-4 (IL-4), and IL-β are released and monocytes begin to infiltrate the implanted site and differentiate into macrophages (41, 55, 56). Reducing FBR has been a challenge because excessive FBRs cause acute and chronic inflammation, which can lead to deadly complications. To assess the effects of bacterial infection in the surrounding tissues of the bare implants and LOIS, hematoxylin and eosin (H&E) and Masson's trichrome (MT) staining were used. For the rabbit that was implanted with bare substrate, serious bacterial infection progressed, and the H&E tissue slide clearly demonstrated the presence of an inflammation-induced abscess and necrosis. On the other hand, the extreme antibiofouling surface, LOIS, inhibited the bacterial adhesion, thus showing no signs of infection and reduced inflammation (Fig. 5C). MT staining results demonstrated the same tendency; however, the MT staining additionally displayed edema in the rabbits implanted with LOIS, suggesting that recovery was about to
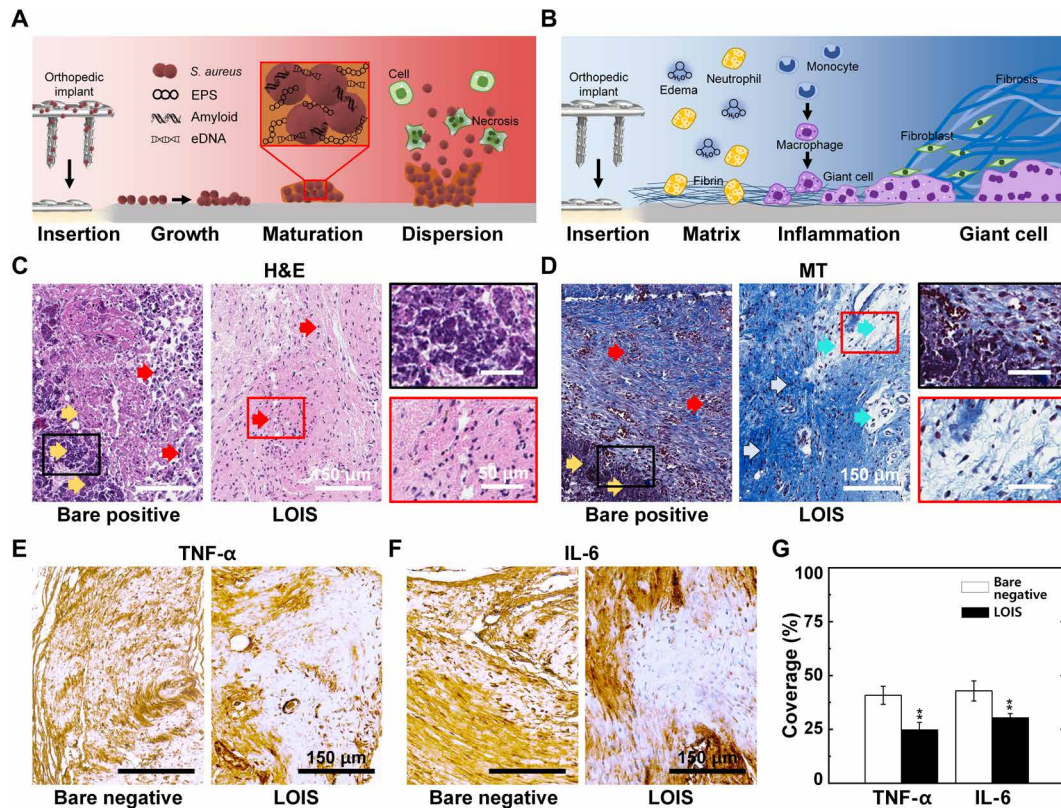
Fig. 5. Histological analysis of tissues surrounding implants incubated in bacterial suspension for 12 hours. (**A**) Schematics of the biofilm formation and spreading mechanism on the infected orthopedic implant's surface. eDNA, extracellular DNAs. (**B**) Schematics of immune response upon the orthopedic implants' insertion. (**C**) H&E staining and (**D**) MT staining of the tissues around the orthopedic implants of bare positive and LOIS. IHC of immune-related cytokines, (**E**) TNF-α and (**F**) IL-6, staining images of the rabbit implanted with bare negative and LOIS. (**G**) Quantification of the cytokine expression via area coverage measurements (**$P < 0.01$).

take place (Fig. 5D). To investigate the degree of the immune response, immunohistochemistry (IHC) staining was done using immune response–related cytokines, TNF-α and IL-6. The bare-negative implants that were not exposed to the bacteria and the LOIS that were exposed to the bacteria but not infected were compared to investigate healing process in the absence of bacterial infection. Figure 5E demonstrates the optical images of the IHC slides expressing TNF-α. The brown-stained area represents the immune response, suggesting slightly reduced immune response in LOIS. In addition, IL-6 expression in LOIS was evidently less compared to the expression in sterilized bare negative (Fig. 5F). The cytokine expression was quantified by measuring the area stained by the antibody corresponding to the cytokines (Fig. 5G). The expression levels measured in rabbits implanted with LOIS were lower compared to the rabbits with bare-negative implants showing meaningful differences. The decreased expression of the cytokines suggests that the long-term, stable antibiofouling property of LOIS is not only related to the inhibition of bacterial infection but also to the reduction in FBR, which was induced by macrophages that adhered to the substrate (53, 57, 58). Therefore, the reduced immune response due to the immune-evasive property of LOIS might resolve side effects following implantation, such as an excessive immune response after orthopedic surgeries.

Biocompatibility of LOIS and its impact on the bone healing process was examined in vivo using diagnostic imaging [x-ray and micro–computed tomography (CT)] and IHC of osteoclasts. Figure 6A demonstrates the bone healing process with three different stages involved: inflammatory stage, repair stage, and remodeling stage. When the bone fracture occurs, inflammatory cells and fibroblasts infiltrate into the fractured bone and start the ingrowth of vascular tissue. In the repair stage, the ingrowth of the vascular tissue proceeds to spread near the fracture site. The vascular tissue provides nutrition for the formation of new bones called callus. The last stage of the bone healing process is the remodeling stage where the size of the callus is reduced to that of a normal bone with the help of the increased levels of activated osteoclasts (59). The fracture site was three-dimensionally (3D) reconstructed using a micro-CT scan to observe the difference in the levels of callus formation for each group. The cross section of the femur was visualized to observe the thickness of the callus around the fractured bone (Fig. 6, B and C). The fracture sites of all groups were also investigated every week using an x-ray to observe the different bone regeneration processes in each group (fig. S9). The callus and the mature bone were represented in blue/green and ivory colors, respectively. Most of the soft tissues were filtered out with a preset threshold. Bare positive and SHP demonstrated a small amount of callus formation around the fracture site. On the other hand, the bare-negative and fracture sites of LOIS were surrounded by a thick layer of callus. The micro-CT images suggest that the formation of callus was hindered by bacterial infection and infection-associated inflammation. This is because the immune system prioritizes the healing of septic injury caused by infection-associated inflammation over bone recovery (60). IHC
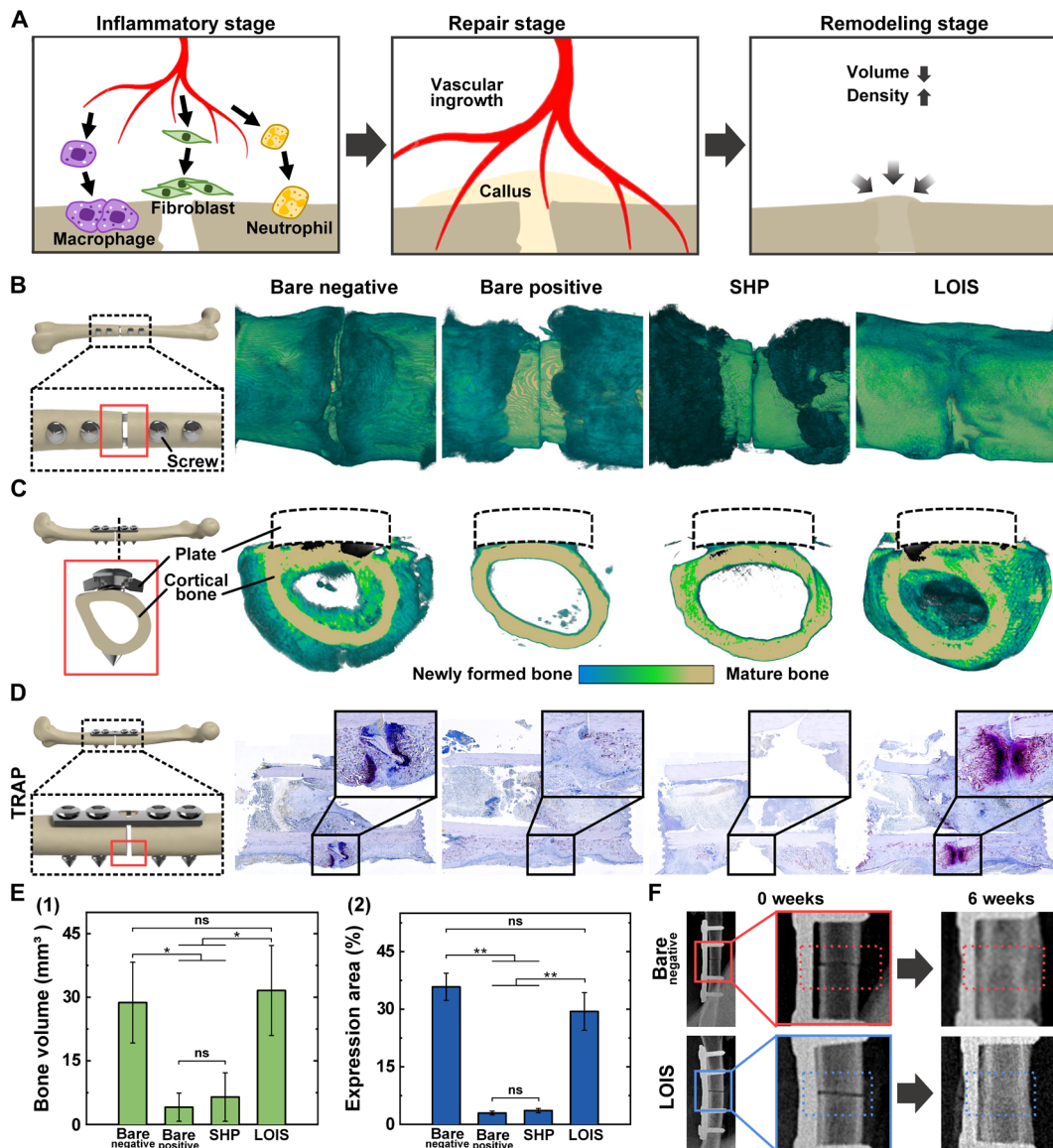
Fig. 6. Analysis of the bone healing process based on micro-CT scan images and TRAP staining. (**A**) Schematics of the bone healing process after fracture. (**B**) Difference in the degrees of callus formation and (**C**) cross-sectional images of the fracture site for each surface group. (**D**) TRAP staining to visualize osteoclast activity and bone resorption. Quantitative analysis of the callus formation outside of the cortical bone with (**E**) (1) micro-CT and (2) osteoclast activity based on TRAP activity. (**F**) X-ray images of the fractured bone of bare negative (highlighted with red dotted rectangle) and LOIS (highlighted with blue dotted rectangle) after 6 weeks of implantation. Statistical analysis was performed via one-way analysis of variance (ANOVA). *$P < 0.05$. **$P < 0.01$.

and tartrate-resistant acid phosphatase (TRAP) staining were performed to visualize the osteoclast activity and bone resorption (Fig. 6D) (61). Only a few activated osteoclasts, which were stained in purple, were found in bare positive and SHP. On the other hand, numerous activated osteoclasts were observed close to the mature bone of the bare positive and LOIS. The phenomenon suggests that callus around the fracture site is in a vigorous remodeling process in the presence of osteoclasts (62). The micro-CT scan and IHC results were quantified by measuring the callus bone volume and osteoclast expression area to compare the level of callus formation around the fracture site in all groups (Fig. 6E, 1 and 2). As expected, the callus formation was significantly higher in the bare negative and LOIS compared to the other groups, suggesting the occurrence of active

bone remodeling (63). Figure S10 demonstrates the optical images of the surgical site, MT staining results of tissues collected near the screws, and TRAP staining results highlighting the screw-bone interface. In the bare substrate, intense callus and fibrosis formation was observed, while the LOIS-treated implant showed a relatively unadhered surface. Similar to, somewhat, lower fibrosis was observed in rabbits implanted with LOIS compared to bare negative, as marked with white arrows. In addition, robust edema (blue arrows) can be attributed to the immune-evasive properties of LOIS, resulting in less severe inflammation. Nonadhered surface and decreased fibrosis surrounding the implants suggest an easier removal process, which often cause additional fracture or inflammation after the removal. The bone healing process after screw removal

was evaluated via osteoclast activity at the screw-bone interface. Similar levels of osteoclasts were recruited to the interface of both bare and LOIS implants for further bone healing, which suggest that the LOIS coating has no negative effects on bone healing or immune response. To confirm that surface modification done on LOIS did not interfere with the bone healing process, the bone healing of the rabbits implanted with bare negative and LOIS for 6 weeks was compared using x-ray examination (Fig. 6F). Results showed no visible fracture signs (persistent osteolytic line) in both groups in which LOIS demonstrated the same degree of bone healing compared to that of the noninfected bare-positive group.

DISCUSSION

In summary, LOIS provides a novel strategy for antibacterial infection and an immune-evasive coating for orthopedic implants. The conventional orthopedic implants with SHP functionalization exhibited short-term antibiofouling properties but failed to maintain their properties in the long term. The superhydrophobicity of the substrate traps air bubbles between the bacteria and substrate that forms air pockets, preventing bacterial infection. However, these air pockets are easily removed due to diffusion of air gases. On the other hand, LOIS well demonstrated its capability of preventing biofilm-related infection, thus the infection-related inflammation due to antirepellent properties of the lubricant layer infused in the hierarchical micro/nanostructured surface. Various characterization methods including SEM, AFM, XPS, and CA measurements were used to optimize the fabrication condition of LOIS. In addition, LOIS was able to be applied to various biomaterials such as PLGA, Ti, PE, POM, and PPSU, which are commonly used in orthopedic fixation devices. LOIS was then tested in vitro to demonstrate its antibiofouling property against bacteria and immune response–related biosubstances. The results showed excellent antibacterial and antibiofouling effects compared to that of the bare implant. Moreover, LOIS showed mechanical robustness even after applying mechanical stress, which is inevitable during orthopedic surgery. Because of the self-healing property of lubricants in micro/nanostructured surfaces, LOIS successfully maintained its antibiofouling property. To investigate the biocompatibility and antibacterial property of LOIS in vivo, the LOIS was implanted on the rabbit's femur for 4 weeks. Bacterial infection was not observed in the rabbits implanted with LOIS. In addition, reduced levels of local immune response were confirmed using IHC, suggesting that the LOIS does not inhibit the bone healing processes. LOIS demonstrated superior antibacterial and immune-evasive properties and proved to be effective for prevention of biofilm formation before and during orthopedic surgical procedures, especially for osteosynthesis. By using the osteomyelitis femoral fracture model of rabbits, the influences of biofilm-related infection to the bone healing processes induced by preincubated implants was studied in depth. As a future study, a new in vivo model that could investigate possible infection after the implantation is required to fully understand and prevent the biofilm-related infection throughout the healing processes. In addition, osteoinduction still remains as an unmet challenge for LOIS to be integrated with. Further research is required to integrate the selective adhesion of osteoinductive cells or regenerative medicine with LOIS to overcome the challenges. Overall, LOIS represents a promising orthopedic implant coating with mechanical robustness and excellent antibiofouling properties for reducing SSI and immune side effects.

MATERIALS AND METHODS

Fabrication of LOIS

The 304 SS substrates in the form of 15 mm by 15 mm by 1 mm (Dong Kang M-Tech Co., Korea) were sequentially cleaned in acetone, EtOH, and DI water for 15 min to remove contaminants. To form micro/nano-hierarchical structures on the surface, the cleaned substrates were immersed in 48 to 51% HF solution (DUKSAN Corp., Korea) at 50°C with varying etching time from 0 to 60 min. The etched substrates were then cleaned with DI water and placed in 65% HNO_3 (DUKSAN Corp., Korea) solution at 50°C for 30 min to generate a chromium oxide passivation layer onto the surface. After the passivation, the substrates were washed using DI water and dried to obtain hierarchically structured substrates. Next, the substrates were exposed to oxygen plasma (100 W, 3 min) and immediately immersed in 8.88 mM solution of POTS (Sigma-Aldrich, Germany) in toluene for 12 hours at room temperature. Then, POTS-coated substrates were cleaned with EtOH and annealed at 150°C for 2 hours to obtain a dense POTS SAM. After the SAM coating, the lubricant layer was formed onto the substrate by applying perfluoropolyether lubricants (Krytox 101; DuPont, USA) with a loading volume of 20 $\mu m/cm^2$. The lubricant was filtered through a 0.2-μm filter before the application. Excessive lubricants were removed by tilting at an angle of 45° for 15 min. Same fabrication procedures were applied to the orthopedic implants (locking plates and cortical locking screws; Dong Kang M-Tech Co., Korea), which were made of 304 SS. All orthopedic implants were designed to be fit into a rabbit femur geometry.

Surface characterization

Surface morphology of substrates and orthopedic implants were examined by field-emission SEM (Inspect F50, FEI, USA) and AFM (XE-100, Park Systems, Korea). The surface roughness (R_a, R_q) was measured by measuring an area of 20 μm by 20 μm ($n = 4$). Surface chemical composition was analyzed using XPS (PHI 5000 VersaProbe, ULVAC PHI, Japan) system equipped with Al K α x-ray source with a 100-μm^2 spot size. Liquid CA and SA were measured using the CA measurement system equipped with a dynamic image capture camera (SmartDrop, FEMTOBIOMED, Korea). For each measurement, 6 to 10 μl of liquid droplet (DI water, horse blood, EG, 30% EtOH, and HD) was placed on the surface to measure CA. SA was measured when the droplets rolled off while the tilting angle of the substrate increased at 2° per s ($n = 4$).

In vitro antibacterial assay

P. aeruginosa [American Type Culture Collection (ATCC) 27853] and MRSA (ATCC 25923) were purchased from the ATCC (Manassas, VA, USA), and the stock culture was maintained at −80°C. Before use, the frozen culture was activated in trypticase soy broth (Komed, Korea) at 37°C with two consecutive transfers after 18 hours of incubation periods. After the incubation, the cultures were centrifuged at 10,000 rpm for 10 min at 4°C and washed twice with a PBS (pH 7.3) solution. The centrifuged cultures were then subcultured onto a blood agar plate (BAP). MRSA and *P. aeruginosa* were prepared overnight and cultured in a Luria-Bertani broth. The concentrations of *P. aeruginosa* and MRSA in the inoculum were confirmed by the CFU quantification of serially diluted suspensions on agar. Then, the bacterial concentration was adjusted to the 0.5 McFarland standard, corresponding to 10^8 CFU/ml. The working bacterial suspension was then diluted 100-fold to 10^6 CFU/ml. To test the

antibacterial adhesion properties, the substrates were sterilized at 121°C for 15 min before use. The substrates were then transferred in a 25-ml bacterial suspension and incubated for 12 and 72 hours with vigorous shaking (200 rpm) at 37°C. After incubation, each substrate was removed from the incubator and washed three times with PBS to remove any floating bacteria on the surface. To observe the biofilm on the substrate, the biofilm was fixed with methanol and stained using 1 ml of acridine orange for 2 min. The stained biofilm was then photographed using the fluorescence microscope (BX51TR, Olympus, Japan). To quantify the biofilm on the substrate, detachment of the attached cells from the substrate was performed by the bead vortexing method, which is considered to be the most suitable method for the removal of the attached bacteria ($n = 4$). Using the sterile forceps, the substrates were taken out from the growth medium and tapped against the well plate to remove excess liquids. Loosely attached cells were removed by rinsing twice with sterile PBS. Each substrate was then transferred to a sterile test tube containing 9 ml of 0.1% peptone saline water (PSW) and 2 g of 20 to 25 sterile glass beads (0.4 to 0.5 mm in diameter). It was subsequently vortexed for 3 min to detach the cells from the coupon. After vortexing, 10-fold serial dilutions of the suspension with 0.1% PSW were made, and 0.1 ml of each dilution was plated onto BAP. After incubation at 37°C for 24 hours, the counting of CFU was manually performed.

In vitro assay against biosubstances
For the cells, mouse fibroblast NIH/3T3 (CRL-1658; ATCC, USA) and mouse macrophage RAW 264.7 (TIB-71; ATCC, USA) were used. The mouse fibroblasts were cultured using Dulbecco's modified Eagle's medium (DMEM; LM001-05, Welgene, Korea) and was supplemented with 10% bovine calf serum (S103-01, Welgene) and 1% penicillin-streptomycin (PS; LS202-02, Welgene). Mouse macrophages were cultured using DMEM and was supplemented with 10% fetal bovin serum (S001-01, Welgene) and 1% PS. The substrates were placed in a six-well cell culture plate, and the cells were seeded at 10^5 cells/cm^2. The cells were incubated overnight at 37°C and 5% CO_2 condition. For the cell staining, the cells were fixed with 4% paraformaldehyde for 20 min and were incubated in 0.5% Triton X-100 for 5 min. The substrates were immersed in 50 nM tetramethylrhodamine at 37°C for 30 min. After the incubation process, the substrates were mounted with VECTASHIELD mounting medium with 4′,6-diamino-2-phenylindole (H-1200, Vector Laboratories, UK) ($n = 4$ for each cell). For the proteins, fluorescein, fluorescein isothiocyanate–albumin (A9771, Sigma-Aldrich, Germany), and fibrinogen from human plasma Alexa Fluor 488 conjugated (F13191, Invitrogen, USA) were dissolved separately in PBS (10 mM, pH 7.4) with an albumin and fibrinogen concentration of 1 and 150 μg/ml, respectively. Before immersing the substrates in the protein solutions, they were rinsed with PBS to rehydrate the surfaces. All the substrates were then immersed in the six-well plates filled with protein solutions separately and were incubated at 37°C for 30 and 90 min. After the incubation, the substrates were then removed from the protein solutions, gently washed three times with PBS, and fixed with 4% paraformaldehyde ($n = 4$ for each protein). For the calcium, sodium chloride (0.21 M) and potassium phosphate (3.77 mM) were dissolved in DI water. By adding a hydrochloride solution (1 M), the pH of the solution adjusted to 2.0. Calcium chloride (5.62 mM) was then dissolved in the solution. The pH of the solution adjusted to 7.4 by the addition of 1 M tris(hydroxymethyl)-aminomethane. All the substrates were immersed in the six-well plates filled with

calcium 1.5× calcium phosphate solution and removed from the solution after 30 min. For the staining, mix the 2 g of Alizarin Red S (C.I. 58005) and 100 ml of DI water. Then, the pH was adjusted to 4 using 10% ammonium hydroxide. Stain the substrates with the Alizarin Red solution for 5 min and shake off excess dye and blot section. After the shaking process, the substrates were dehydrated and immersed in acetone for 5 min and then in acetone-xylene (1:1) solution for 5 min and, last, rinsed using xylene ($n = 4$). All substrates were imaged using fluorescence microscopy (Axio Imager. A2m, Zeiss, Germany) with a ×10 and ×20 objective. ImageJ/FIJI (https://imagej.nih.gov/ij/) was used to quantify the biosubstances adhesion data on four different imaging areas from each group. All images were converted into binary images with a fixed threshold to enable substrate comparison.

Analysis for the stability of the lubricant layer under flow
Stability of the lubricant layer in PBS was monitored using a Zeiss LSM 700 confocal microscope in reflection mode. Fluorine-based SAM-coated glass samples with infused lubricant layer were submerged in PBS solution and tested in mild shaking conditions (120 rpm) using orbital shaker (SHO-1D; Daihan Scientific, Korea). The samples were then taken out, and the loss of lubricant was monitored by measuring a loss of reflected light. To acquire the fluorescence images in reflection mode, the samples were exposed to 633-nm laser light, which was then collected, as the light reflected off the sample. Samples were measured in the time interval of 0, 30, 60, and 120 hours.

Mechanical characterization of orthopedic implants
To determine the effects of the surface modification process on the nanomechanical properties of orthopedic implants, nanoindentaion measurements were carried out using a nanoindenter (TI 950 TriboIndenter, Hysitron, USA), which was equipped with a three-sided pyramidal Berkovich diamond tip. The peak load was 10 mN, and the area was 100 μm by 100 μm. For all measurements, the loading and unloading times were 10 s, and the holding time was 2 s at the peak indent loads. The measurements were conducted from five different locations and were averaged. To evaluate the mechanical strength properties under load, transverse three-point bending tests were carried out using a universal testing machine (Instron 5966, Instron, USA). The compression was applied on the substrate with an increasing load at a constant rate of 10 N/s. The bending modulus and maximum compressive stress were calculated using the Bluehill Universal software program ($n = 3$).

Ex vivo experiments
To simulate the surgical procedure and related mechanical damages induced during the surgery, the surgical procedure was performed ex vivo. The femurs were collected from sacrificed New Zealand white rabbits. The femur was cleaned and fixed in 4% paraformaldehyde for 1 week. The surgical procedure was done on fixed femurs, as described in the animal experiment methods. After the procedure, the orthopedic implants were immersed in the blood (horse blood, KISAN, Korea) for 10 s to confirm the occurrence of blood adhesion after mechanical damages were applied ($n = 3$).

In vivo rabbit femur fracture model of implant-associated infection
A total of 24 male New Zealand white rabbits (3.0 to 3.5 kg in weight, average age of 6 months) were randomly divided into four

groups: bare negative, bare positive, SHP, and LOIS. All procedures involving animals were performed in accordance with the ethical standards of the Institutional Animal Care and Use Committee (IACUC approval, KOREA-2017-0159). Orthopedic implants including locking plates (41 mm in length, 7 mm in width, and 2 mm in thickness) with five holes and cortical locking screws (12 mm in length and 2.7 mm in diameter) were used for fracture fixation. All plates and screws, except for those used in the bare-negative group, were incubated in a MRSA suspension (10^6 CFU/ml) for 12 hours. The bare-negative group ($n = 6$) was treated with bare surface implants without being exposed to bacterial suspension, as a negative control of infection. The bare-positive group ($n = 6$) was treated with bare surface implants with bacterial exposure, as a positive control of infection. The SHP group ($n = 6$) was treated with SHP implants with bacterial exposure. Last, the LOIS group ($n = 6$) was treated with the LOIS implant with bacterial exposure. All animals were kept in a single cage and supplied with plenty of food and water. Before surgery, the rabbits were fasted for 12 hours. The animals were anesthetized using an intramuscular injection of xylazine (5 mg/kg) and intravenous injection of alfaxalone (3 mg/kg) for induction. Afterward, 2% isoflurane and 50 to 70% of medical oxygen (2 L/min of flow) were delivered through the respiratory system to maintain anesthesia. Implantation was performed via a direct lateral approach to the femur. After removing the hair and sterilizing the skin with povidone-iodine, an approximately 6-cm-long incision was made at the lateral aspect of the middle left femur. The femur was completely exposed by opening the gap between the muscles covering the femur. The plate was placed in front of the femoral shaft and fixed with four screws. After fixation, a fracture was created artificially at the area between the second and fourth hole by using a saw blade (1 mm thick). At the end of the operation, the wound was rinsed with saline and closed in layers with sutures. Every rabbit was treated with a subcutaneous injection of enrofloxacin (5 mg/kg) diluted one-third in normal saline. Postoperative x-rays of the femur were taken in all animals (0, 7, 14, 21, 28, and 42 days) to confirm the osteotomy of the bone. All animals were sacrificed at days 28 and 42 using an intravenous injection of KCl (2 mmol/kg) after deep anesthesia. After sacrifice, a micro-CT scan was performed on the femur to observe and compare the bone healing process and new bone formation between the four groups.

Histological and IHC examinations

Soft tissues, which were directly in contact with orthopedic implants, were collected after sacrifice. The tissues were fixed overnight in 10% neutral-buffered formalin, followed by dehydration in EtOH. The dehydrated tissues were embedded in paraffin and sectioned at 40 μm thickness by using a microtome (400CS; EXAKT, Germany). To visualize the infection, H&E staining and MT staining were performed. To examine the host response, the sectioned tissues were incubated with primary antibodies against rabbit anti–TNF-α (AB6671, Abcam, USA), rabbit anti–IL-6 (AB6672; Abcam, USA) followed by incubation in secondary antibodies conjugated with horseradish peroxidase. According to the instructions of the manufacturer, Avidin-Biotin Complex (ABC) staining system was applied to the sections. To appear as a brown reaction product, 3,3-diaminobenzidine was used in all sections. All sections were visualized using a digital slide scanner (Pannoramic 250 Flash III, 3DHISTECH, Hungary), and at least four substrates per group were analyzed by ImageJ software.

X-ray and micro-CT

X-ray images were taken in all animals after surgery and every week thereafter to monitor the bone fracture healing ($n = 6$ per group). After the sacrifice, high-resolution micro-CT was taken to calculate the callus formation around the healed femur. The obtained femurs were cleaned, fixed in 4% paraformaldehyde for 3 days, and dehydrated in 75% EtOH. Dehydrated bones were then scanned by using micro-CT (SkyScan 1173, Bruker microCT, Kontich, Belgium) to generate 3D voxel images (2240 × 2240 pixels) of the bone samples. An Al 1.0-mm filter was used to reduce signal noise, and high resolution ($E = 133$ kVp, $I = 60$ μA, integration time = 500 ms) was applied to all scans. The 3D volumes of the scanned samples were generated from the acquired 2D lateral projections using the Nrecon software (version 1.6.9.8, Bruker microCT, Kontich, Belgium). For the analysis, 3D reconstructed images were divided into a cube of 10 mm by 10 mm by 10 mm on the basis of the fracture site. The callus on the outside of the cortical bone was calculated. The scanned bone volumes were digitally reoriented using the DataViewer (version 1.5.1.2; Bruker microCT, Kontich, Belgium) software, and analyzed using the CT-Analyzer (version 1.14.4.1; Bruker microCT, Kontich, Belgium) software. The relative x-ray absorption coefficients within mature bone and callus were distinguished by its density, and the volume of callus was then quantified ($n = 4$). To confirm that the biocompatibility of LOIS does not delay the bone healing process, additional x-ray and micro-CT analysis were carried out in two rabbits: bare-negative and LOIS group. Both groups were sacrificed in week 6.

TRAP staining

Femurs from the sacrificed animals were collected and fixed in 4% paraformaldehyde for 3 days. The orthopedic implants were then carefully removed from the femur. Femurs were decalcified by using 0.5 M EDTA (EC-900, National Diagnostics, USA) for 21 days. The decalcified femurs were then dehydrated by immersing them in EtOH. The dehydrated femurs were cleared in xylene and embedded in paraffin. Samples were then sectioned with Automated Rotary Microtome (Leica RM2255, Leica Biosystems, Germany) at a thickness of 3 μm. For TRAP staining (F6760, Sigma-Aldrich, Germany), the sectioned samples were dewaxed, rehydrated, and incubated in the TRAP reagent for 1 hour at 37°C. The images were acquired using a slide scanner (Pannoramic 250 Flash III, 3DHISTECH, Hungary) and quantified by measuring the area coverage of the stained area. At least four substrates per group were analyzed by ImageJ software in each experiment.

Statistical analysis

Statistical significance was performed by using GraphPad Prism (GraphPad Software Inc., USA). The differences between groups were assessed with the unpaired t test and one-way analysis of variance (ANOVA) test. The levels of significance are indicated in the figures and as follows: *$P < 0.05$, **$P < 0.01$, ***$P < 0.001$, and ****$P < 0.0001$; NS, no significant difference.

SUPPLEMENTARY MATERIALS

Supplementary material for this article is available at http://advances.sciencemag.org/cgi/content/full/6/44/eabb0025/DC1

View/request a protocol for this paper from *Bio-protocol*.

REFERENCES AND NOTES

1. E. White, D. Lu, B. Eyer, C. Gottsegen, E. Ahlmann, C. Allison, Gallery of uncommon orthopedic implants: A guide for emergency radiologist. *Emerg. Radiol.* **17**, 227–247 (2010).

2. F. Barrère, T. A. Mahmood, K. De Groot, C. A. Van Blitterswijk, Advanced biomaterials for skeletal tissue regeneration: Instructive and smart functions. *Mater. Sci. Eng. R Rep.* **59**, 38–71 (2008).

3. S. Wu, X. Liu, K. W. K. Yeung, C. Liu, X. Yang, Biomimetic porous scaffolds for bone tissue engineering. *Mater. Sci. Eng. R Rep.* **80**, 1–36 (2014).

4. L. Rony, R. Lancigu, L. Hubert, Intraosseous metal implants in orthopedics: A review. *Morphologie* **102**, 231–242 (2018).

5. J. W. Costerton, P. S. Stewart, E. P. Greenberg, Bacterial biofilms: A common cause of persistent infections. *Science* **284**, 1318–1322 (1999).

6. D.-W. Lee, Y.-P. Yun, K. Park, S. E. Kim, Gentamicin and bone morphogenic protein-2 (BMP-2)-delivering heparinized-titanium implant with enhanced antibacterial activity and osteointegration. *Bone* **50**, 974–982 (2012).

7. P. Stoodley, S. Kathju, F. Z. Hu, G. Erdos, J. E. Levenson, N. Mehta, B. Dice, S. Johnson, L. Hall-Stoodley, L. Nistico, N. Sotereanos, J. Sewecke, J. C. Post, G. D. Ehrlich, Molecular and imaging techniques for bacterial biofilms in joint arthroplasty infections. *Clin. Orthop. Relat. Res.* **437**, 31–40 (2005).

8. Z. Feng, X. Liu, L. Tan, Z. Cui, X. Yang, Z. Li, Y. Zheng, K. W. K. Yeung, S. Wu, Electrophoretic deposited stable Chitosan@MoS$_2$ coating with rapid in situ bacteria-killing ability under dual-light irradiation. *Small* **14**, 1704347 (2018).

9. L. Zhang, C. Ning, T. Zhou, X. Liu, K. W. K. Yeung, T. Zhang, Z. Xu, X. Wang, S. Wu, P. K. Chu, Polymeric nanoarchitectures on ti-based implants for antibacterial applications. *ACS Appl. Mater. Interfaces* **6**, 17323–17345 (2014).

10. L. S. M. Gomes, Early diagnosis of periprosthetic joint infection of the hip-current status, advances, and perspectives. *Rev. Bras. Ortop.* **54**, 368–376 (2019).

11. L. Zhang, J. Yan, Z. Yin, C. Tang, Y. Guo, D. Li, B. Wei, Y. Xu, Q. Gu, L. Wang, Electrospun vancomycin-loaded coating on titanium implants for the prevention of implant-associated infections. *Int. J. Nanomedicine* **9**, 3027–3036 (2014).

12. T. Fuchs, R. Stange, G. Schmidmaier, M. J. Raschke, The use of gentamicin-coated nails in the tibia: Preliminary results of a prospective study. *Arch. Orthop. Trauma Surg.* **131**, 1419–1425 (2011).

13. K. Inoue, K. Mitsudo, M. Nobuyoshi, Medial necrosis due to sirolimus-eluting stent implantation in human coronary artery. *J. Cardiol.* **51**, 60–64 (2008).

14. K. Ohyama, Y. Matsumoto, H. Amamizu, H. Uzuka, K. Nishimiya, S. Morosawa, M. Hirano, H. Watabe, Y. Funaki, S. Miyata, J. Takahashi, K. Ito, H. Shimokawa, Association of coronary perivascular adipose tissue inflammation and drug-eluting stent–induced coronary hyperconstricting responses in pigs: ^{18}F-fluorodeoxyglucose positron emission tomography imaging study. *Arterioscler. Thromb. Vasc. Biol.* **37**, 1757–1764 (2017).

15. M. Champeau, J.-M. Thomassin, T. Tassaing, C. Jérôme, Drug loading of polymer implants by supercritical CO$_2$ assisted impregnation: A review. *J. Control. Release* **209**, 248–259 (2015).

16. T. Hoare, J. Santamaria, G. F. Goya, S. Irusta, D. Lin, S. Lau, R. Padera, R. Langer, D. S. Kohane, A magnetically triggered composite membrane for on-demand drug delivery. *Nano Lett.* **9**, 3651–3657 (2009).

17. K. Y. Lee, D. J. Mooney, Hydrogels for tissue engineering. *Chem. Rev.* **101**, 1869–1880 (2001).

18. G. Cheng, G. Li, H. Xue, S. Chen, J. D. Bryers, S. Jiang, Zwitterionic carboxybetaine polymer surfaces and their resistance to long-term biofilm formation. *Biomaterials* **30**, 5234–5240 (2009).

19. X. Xie, J. C. Doloff, V. Yesilyurt, A. Sadraei, J. J. McGarrigle, M. Omami, O. Veiseh, S. Farah, D. Isa, S. Ghani, I. Joshi, A. Vegas, J. Li, W. Wang, A. Bader, H. H. Tam, J. Tao, H.-j. Chen, B. Yang, K. A. Williamson, J. Oberholzer, R. Langer, D. G. Anderson, Reduction of measurement noise in a continuous glucose monitor by coating the sensor with a zwitterionic polymer. *Nat. Biomed. Eng.* **2**, 894–906 (2018).

20. F. Faÿ, I. Linossier, J. J. Peron, V. Langlois, K. Vallée-Rehel, Antifouling activity of marine paints: Study of erosion. *Prog. Org. Coat* **60**, 194–206 (2007).

21. Y. Zhang, W. He, J. Li, K. Wang, J. Li, H. Tan, Q. Fu, Gemini quaternary ammonium salt waterborne biodegradable polyurethanes with antibacterial and biocompatible properties. *Mater. Chem. Front* **1**, 361–368 (2017).

22. A. Göpferich, Mechanisms of polymer degradation and erosion. *Biomaterials* **17**, 103–114 (1996).

23. S. H. Choi, J. H. Lee, Absorbable plate-related infection after facial bone fracture reduction. *Arch Craniofac Surg.* **17**, 1–4 (2016).

24. L. Feng, S. Li, Y. Li, H. Li, L. Zhang, J. Zhai, Y. Song, B. Liu, L. Jiang, D. Zhu, Super-hydrophobic surfaces: From natural to artificial. *Adv. Mater.* **14**, 1857–1860 (2002).

25. E. Celia, T. Darmanin, E. Taffin De Givenchy, S. Amigoni, F. Guittard, Recent advances in designing superhydrophobic surfaces. *J. Colloid Interface Sci.* **402**, 1–18 (2013).

26. P. Tang, W. Zhang, Y. Wang, B. Zhang, H. Wang, C. Lin, L. Zhang, Effect of superhydrophobic surface of titanium on *Staphylococcus aureus* adhesion. *J. Nanomater.* **2011**, 8 (2011).

27. M. A. Samaha, H. V. Tafreshi, M. Gad-El-Hak, Influence of flow on longevity of superhydrophobic coatings. *Langmuir* **28**, 9759–9766 (2012).

28. G. B. Hwang, K. Page, A. Patir, S. P. Nair, E. Allan, I. P. Parkin, The anti-biofouling properties of superhydrophobic surfaces are short-lived. *ACS Nano* **12**, 6050–6058 (2018).

29. C. Howell, T. L. Vu, J. J. Lin, S. Kolle, N. Juthani, E. Watson, J. C. Weaver, J. Alvarenga, J. Aizenberg, Self-replenishing vascularized fouling-release surfaces. *ACS Appl. Mater. Interfaces* **6**, 13299–13307 (2014).

30. N. Vogel, R. A. Belisle, B. Hatton, T.-S. Wong, J. Aizenberg, Transparency and damage tolerance of patternable omniphobic lubricated surfaces based on inverse colloidal monolayers. *Nat. Commun.* **4**, 2176 (2013).

31. L. Li, V. Breedveld, D. W. Hess, Creation of superhydrophobic stainless steel surfaces by acid treatments and hydrophobic film deposition. *ACS Appl. Mater. Interfaces* **4**, 4549–4556 (2012).

32. P. Kim, M. J. Kreder, J. Alvarenga, J. Aizenberg, Hierarchical or not? Effect of the length scale and hierarchy of the surface roughness on omniphobicity of lubricant-infused substrates. *Nano Lett.* **13**, 1793–1799 (2013).

33. U. Bauer, W. Federle, The insect-trapping rim of nepenthes pitchers: Surface structure and function. *Plant Signal. Behav.* **4**, 1019–1023 (2009).

34. S. Mattaparthi, C. S. Sharma, Fabrication of self-cleaning antireflective polymer surfaces by mimicking underside leaf hierarchical surface structures. *J. Bionic. Eng.* **16**, 400–409 (2019).

35. T.-S. Wong, S. H. Kang, S. K. Y. Tang, E. J. Smythe, B. D. Hatton, A. Grinthal, J. Aizenberg, Bioinspired self-repairing slippery surfaces with pressure-stable omniphobicity. *Nature* **477**, 443–447 (2011).

36. G. Li, G. Yang, P. Zhang, Y. Li, J. Meng, H. Liu, S. Wang, Rapid cell patterning induced by differential topography on silica nanofractal substrates. *Small* **11**, 5642–5646 (2015).

37. R. Y. Pelgrift, A. J. Friedman, Nanotechnology as a therapeutic tool to combat microbial resistance. *Adv. Drug Del. Rev.* **65**, 1803–1815 (2013).

38. W. Hou, X. Sun, Z. Wang, Y. Zhang, Biofilm-forming capacity of *staphylococcus epidermidis*, *staphylococcus aureus*, and *pseudomonas aeruginosa* from ocular infections. *Invest. Ophthalmol. Visual Sci.* **53**, 5624–5631 (2012).

39. M. Choi, L. Xiangde, J. Park, D. Choi, J. Heo, M. Chang, C. Lee, J. Hong, Superhydrophilic coatings with intricate nanostructure based on biotic materials for antifogging and antibiofouling applications. *Chem. Eng. J.* **309**, 463–470 (2017).

40. T. P. Nhung Nguyen, P. Brunet, Y. Coffinier, R. Boukherroub, Quantitative testing of robustness on superomniphobic surfaces by drop impact. *Langmuir* **26**, 18369–18373 (2010).

41. J. M. Anderson, A. Rodriguez, D. T. Chang, Foreign body reaction to biomaterials. *Semin. Immunol.* **20**, 86–100 (2008).

42. L. Tang, J. W. Eaton, Fibrin(ogen) mediates acute inflammatory responses to biomaterials. *J. Exp. Med.* **178**, 2147–2156 (1993).

43. N. Y. Kostina, C. Rodriguez-Emmenegger, M. Houska, E. Brynda, J. Michálek, Non-fouling hydrogels of 2-hydroxyethyl methacrylate and zwitterionic carboxybetaine (meth) acrylamides. *Biomacromolecules* **13**, 4164–4170 (2012).

44. Y.-N. Chou, F. Sun, H.-C. Hung, P. Jain, A. Sinclair, P. Zhang, T. Bai, Y. Chang, T.-C. Wen, Q. Yu, S. Jiang, Ultra-low fouling and high antibody loading zwitterionic hydrogel coatings for sensing and detection in complex media. *Acta Biomater.* **40**, 31–37 (2016).

45. M. S. Konsta-Gdoutos, Z. S. Metaxa, S. P. Shah, Multi-scale mechanical and fracture characteristics and early-age strain capacity of high performance carbon nanotube/ cement nanocomposites. *Cem. Concr. Compos.* **32**, 110–115 (2010).

46. H. Fischer, M. Schäfer, R. Marx, Effect of surface roughness on flexural strength of veneer ceramics. *J. Dent. Res.* **82**, 972–975 (2003).

47. O. R. Boughton, S. Ma, S. Zhao, M. Arnold, A. Lewis, U. Hansen, J. P. Cobb, F. Giuliani, R. L. Abel, Measuring bone stiffness using spherical indentation. *PLOS ONE* **13**, e0200475 (2018).

48. D. L. Williams, J. W. Costerton, Using biofilms as initial inocula in animal models of biofilm-related infections. *J. Biomed. Mater. Res. B Appl. Biomater.* **100**, 1163–1169 (2012).

49. J. W. Costerton, Cystic fibrosis pathogenesis and the role of biofilms in persistent infection. *Trends Microbiol.* **9**, 50–52 (2001).

50. X. Zhang, Y.-F. Ma, L. Wang, N. Jiang, C.-H. Qin, Y.-J. Hu, B. Yu, A rabbit model of implant-related osteomyelitis inoculated with biofilm after open femoral fracture. *Exp. Ther. Med.* **14**, 4995–5001 (2017).

51. F. Reffuveille, J. Josse, Q. Vallé, C. Mongaret, S. C. Gangloff, *Staphylococcus aureus Biofilms and their Impact on the Medical Field* (InTech, 2017).

52. J. N. Anderl, M. J. Franklin, P. S. Stewart, Role of antibiotic penetration limitation in *Klebsiella pneumoniae* biofilm resistance to ampicillin and ciprofloxacin. *Antimicrob. Agents Chemother.* **44**, 1818–1824 (2000).

53. W. J. Geelhoed, L. Moroni, J. I. Rotmans, Utilizing the foreign body response to grow tissue engineered blood vessels in vivo. *J. Cardiovasc. Transl. Res.* **10**, 167–179 (2017).

54. F. M. Szaba, S. T. Smiley, Roles for thrombin and fibrin(ogen) in cytokine/chemokine production and macrophage adhesion in vivo. *Blood* **99**, 1053–1059 (2002).

55. B. Johnston, E. C. Butcher, Chemokines in rapid leukocyte adhesion triggering and migration. *Semin. Immunol.* **14**, 83–92 (2002).

56. N. P. Rhodes, J. A. Hunt, D. F. Williams, Macrophage subpopulation differentiation by stimulation with biomaterials. *J. Biomed. Mater. Res.* **37**, 481–488 (1997).

57. P. C. S. Bota, A. M. B. Collie, P. Puolakkainen, R. B. Vernon, E. H. Sage, B. D. Ratner, P. S. Stayton, Biomaterial topography alters healing *in vivo* and monocyte/macrophage activation *in vitro*. *J. Biomed. Mater. Res. A* **95**, 649–657 (2010).

58. T. L. Bonfield, E. Colton, J. M. Anderson, Plasma protein adsorbed biomedical polymers: Activation of human monocytes and induction of interleukin 1. *J. Biomed. Mater. Res.* **23**, 535–548 (1989).

59. I. H. Kalfas, Principles of bone healing. *Neurosurg. Focus* **10**, 1–4 (2001).

60. X. Jin, Y.-H. Xiong, X.-Y. Zhang, R. Wang, Y. Xing, S. Duan, D. Chen, W. Tian, F.-J. Xu, Self-adaptive antibacterial porous implants with sustainable responses for infected bone defect therapy. *Adv. Funct. Mater.* **29**, 1807915 (2019).

61. M. J. Seibel, Biochemical markers of bone turnover: Part i: Biochemistry and variability. *Clin. Biochem. Rev.* **26**, 97–122 (2005).

62. J.-B. Kim, P. Leucht, C. A. Luppen, Y. J. Park, H. E. Beggs, C. H. Damsky, J. A. Helms, Reconciling the roles of fak in osteoblast differentiation, osteoclast remodeling, and bone regeneration. *Bone* **41**, 39–51 (2007).

63. P. Bianco, P. Ballanti, E. Bonucci, Tartrate-resistant acid phosphatase activity in rat osteoblasts and osteocytes. *Calcif. Tissue Int.* **43**, 167–171 (1988).